Mysen *Progress in Earth and Planetary Science* (2018) 5:40
https://doi.org/10.1186/s40645-018-0198-1

Progress in Earth and Planetary Science

RESEARCH ARTICLE Open Access

Silicate solution, cation properties, and mass transfer by aqueous fluid in the Earth's interior

Bjorn Mysen

Abstract

Aqueous fluids in the Earth's interior are multicomponent systems with silicate solubility and solution mechanisms strongly dependent on other dissolved components. Here, solution mechanisms that describe the interaction between dissolved silicate and other solutes were determined experimentally to 825 °C and above 1 GPa with in situ vibrational spectroscopy of aqueous fluid while these were at high temperature and pressure. The silicate content in Na-bearing, silicate-saturated aqueous fluid exceeds that in pure SiO_2 at high temperature and pressure. Silicate species were of Q^0 (isolated SiO_4 tetrahedra) and Q^1 (dimers, Si_2O_7) type. The temperature dependence of its equilibrium constant, $K = X_{Q1}/(X_{Q0})^2$, yields enthalpies of 22 ± 12 and 51 ± 17 kJ/mol for the SiO_2–H_2O and Na-bearing fluids. In contrast, in Ca-bearing fluids, the solubility is more than an order of magnitude lower, and only Q^0 species are present. The present data together with other published experimental information lead to the conclusion that the silicate solubility in aqueous fluids in equilibrium with mafic rocks such as amphibolite and peridotite is an order of magnitude lower than the solubility in fluids in equilibrium with felsic rocks such as andesite and rhyolite compositions (felsic gneiss) under similar temperature and pressure conditions. The silicate speciation also is more polymerized in the felsic systems. This difference is also why second critical end-points in the Earth are at lower temperature and pressure in felsic compared with mafic systems. Alkali-rich fluids formed by dehydration of felsic rocks also show enhanced high field strength element (HFSE) solubility because alkalis in such solution form oxy complexes with the HFSE cations. Fluids formed by dehydration of felsic rocks in the Earth's interior are, therefore, more efficient transport agents of silicate materials than fluids formed by dehydration of mafic and ultramafic rocks, whether for major, minor, or trace elements.

Keywords: Aqueous fluid, Solubility, Structure, Spectroscopy, Silicate

Introduction

The solubility and solution mechanism(s) of silicate components in aqueous fluids in the Earth's interior are central to our understanding of the roles of aqueous fluids in material transport within the Earth (Fockenberg et al. 2006; Newton and Manning 2009; Burchard et al. 2011). This is particularly so in and near subduction zones where water-rich fluids released from dehydrating slab materials can transport chemical components into source regions of melting and, at the same time, deplete dehydrating slab materials of fluid-soluble components (Mibe et al. 2008; Kawamoto et al. 2012). In this environment, hydrated rocks ranging from amphibolite and peridotite to felsic gneiss compositions are subjected to dehydration and release of silicate-saturated water-rich fluids.

The abundance of components known to affect silicate solubility in aqueous fluid differs significantly among those rock types in the Earth's interior. It is necessary, therefore, to determine how individual compositional variables affect the silicate solubility and structure of dissolved silicate in aqueous fluids at relevant high-temperature and high-pressure conditions.

Composition and structure of silicate-saturated aqueous fluids at high temperature and pressure have been determined experimentally for pure SiO_2–H_2O systems as well as for some more complex silicate and aluminosilicate compositions (Newton and Manning 2002; Kessel et al. 2005; Mibe et al. 2008, 2011; Mysen 2010). From those

Correspondence: bmysen@carnegiescience.edu
Geophysical Laboratory, Carnegie Institution of Washington, Washington, DC, USA

experiments, it is evident that silicate solubility in aqueous fluids depends on the presence of other components in addition to SiO_2. In the $MgO–SiO_2–H_2O$ system, for example, the solubility in the aqueous fluid decreases with increasing Mg/Si abundance ratio (Zhang and Frantz 2000). Addition of aluminosilicate components to SiO_2 also enhances the solubility in fluid (Wilke et al. 2012). However, quantitative characterization of how individual components affect silicate solubility and solution mechanisms of other components in aqueous fluids is not well developed.

Determination of fluid composition and structure at temperature and pressure conditions of the deep crust, upper mantle, and beyond is challenging because silicate-saturated fluids commonly do not retain in solution the chemical components and the fluid structure that existed at the high temperature and pressure after temperature quenching from experimental conditions to ambient temperature and pressure. Various methods have been proposed with which to overcome these obstacles. For example, Kessel et al. (2004) described a method whereby fluids were soaked into layers of pore space among diamond particles during experiments. Analysis of these diamond aggregates after termination of an experiment provided the fluid data. Others rely on accurate weighing of crystals from the experimental charges before and after an experiment at high temperature and pressure during which crystalline material equilibrated with fluid (Manning and Boettcher 1994). The weight difference is the weight of the solute.

An alternative, which does not rely on quenching to ambient conditions before analysis, is to conduct structural characterization of fluids in the equilibrium with one or more condensed phases while at the temperatures and pressures of interest. This can be accomplished with the sample contained in an externally heated hydrothermal diamond anvil cell (Bassett et al. 1993). Here, this experimental protocol was employed to assess the influence of alkalis and alkaline earth cations on SiO_2 solubility in aqueous solutions to temperatures and pressures corresponding to the deep crust and upper mantle.

Methods/Experimental

Three different starting materials were used. Those were crystalline quartz + H_2O, crystalline quartz + 0.7 m NaOH aqueous solution, and an SiO_2 + CaO mixture + H_2O (SiO_2:CaO = 9:1 by mol). By using NaOH as the Na^+-bearing fluid component, it cannot be ruled out that an increased pH compared with pure H_2O could also affect the silicate solubility in the fluid.

The $CaO–SiO_2$ material was prepared by melting at ambient pressure at 1725 °C followed by crystallization at 1500 °C. At 1725 °C, this system comprises immiscible silicate liquids (Osborn and Muan 1960). In order to form the crystalline SiO_2 component desired to equilibrate with fluid, the crystallization step at 1500 °C was performed. This mixture, consisting of crystalline tridymite + glass (Ca-rich) was used together with H_2O as a starting material. During the experiments, tridymite converted to quartz and glass to wollastonite, as discussed further below.

The experiments were carried out in an externally heated, hydrothermal diamond anvil cell (HDAC) of the design originally described by Bassett et al. (1993). In the HDAC, the sample was heated with external heaters. These heaters were comprised of Mo wire wrapped around the SiC diamond seats of upper and lower diamonds that were held in place with alumina high-temperature cement. Iridium gaskets (125 μm thick) with a 500-μm sample hole were employed for sample containment. During an experiment, the gaskets shrunk to about 80 μm thickness and the hole to ~ 400 μm diameter.

MicroRaman spectroscopy and optical microscopy were used to characterize the samples while these were in the HDAC at the pressure/temperature of interest. The Raman system is a JASCO model NRS-3100 confocal microRaman spectrometer with a single monochromator and holographic gratings (1200 and 2400 grooves/mm). A long working distance (25 mm), × 50 magnification, 0.42 N.A. objective lens was used in this design, which provided a better than 5 μm spatial resolution for sample examination and spectroscopic characterization. The sampling depth was about 30 μm (Mysen 2015a). The signals were recorded with an Andor™ Model DV401-F1 1024 × 28 pixel Peltier-cooled CCD (charge-coupled detector). Energy resolution was ± 3 cm^{-1} with 1200 grooves/mm gratings, whereas with 2400 grooves/mm, spectral reproducibility was about 1 cm^{-1}.

Temperatures in the diamond cell were monitored with two K-type thermocouples that touched the diamonds at a ~ 1-mm distance from the sample chamber. A feedback mechanism was utilized for temperature control. Temperature precision was ± 1 °C, whereas the uncertainty, determined against the melting point of NaCl, was 2–3 °C. The gasket hole in the Ir gasket material deformed some during the experiments, which were not, therefore, strictly isochoric. Pressure could not, therefore, be calculated from the PVT data of pure H_2O. Furthermore, silicate components dissolved in the fluid also affect the equation of state of H_2O (Mysen 2010). Instead, the pressure was measured with the one-phonon Raman line from a chip of synthetic carbon-13 diamond placed inside the sample chamber. From this information, the pressure was determined with the calibration of Mysen and Yamashita (2010). An internal standard of Ne emission lines was employed to optimize the energy resolution. With this standard

together with 2400 grooves/mm gratings, a frequency uncertainty of ± 0.1 cm^{-1} was obtained. This uncertainty translates to a pressure precision of ± 40 MPa. However, the overall pressure uncertainty is approximately ± 110 MPa when taking into considerations the uncertainties in the pressure calibration by Mysen and Yamashita (2010).

Several series of measurements at different temperatures and pressures were carried out with the three different starting materials such that for each of the three starting compositions, the sample was first taken to the highest planned temperature and pressure and left there for an hour before spectroscopic measurements. The sample was then cooled at 1 °C/s in 50–75 °C intervals to the next temperature and pressure condition where the spectra were recorded after about 60-minute dwell time. With this sample configuration, the 60-minute dwell time is sufficient to reach equilibrium (Mysen 2015b).

Results

Quartz and aqueous fluid were present in all experiments (Table 1). Additionally, in the system SiO_2–CaO–H_2O, wollastonite coexists with quartz and fluid (Fig. 1). The quartz and wollastonite, identified from their Raman spectra, grew from the starting materials during the initial hour at the highest temperature and pressure. The high-temperature spectra typically are broader and less well resolved compared with the spectra recorded at ambient temperature and pressure (Fig. 2).

The spectra of silicates and fluid at high temperature and pressure show Raman signals in a high-frequency region centered between 3500 and 3600 cm^{-1} and a low-frequency region between 300 and 1200 cm^{-1}. The high-frequency region comprises that of the fundamental O–H vibrations in OH groups, whether in molecular H_2O or as OH groups that form bonding with metal cations (Ratcliffe and Irish 1982; Walrafen et al. 1986). The low-frequency region, between about 300 and 1200 cm^{-1}, includes the Raman bands assigned to vibrations in Si–O, Al–O, and metal oxide components (Brawer and White 1975; McMillan et al. 1992).

The high-frequency region comprises a single slightly asymmetric band. The asymmetry is less pronounced in the spectra from fluid in SiO_2–CaO–H_2O than for the other two compositions (Fig. 3). The low-frequency region characteristically has a strong and sharp band between 770 and 800 cm^{-1} (Fig. 4). In the SiO_2–CaO–H_2O fluid spectra, this is the only Raman band in this frequency region (Fig. 4c), whereas for SiO_2–H_2O and SiO_2–NaOH–H_2O fluids, there is a Raman intensity on both the low- and high-frequency side of 770–800 cm^{-1} peak (Fig. 4a, b). These latter intensities are strongest in the spectra of SiO_2–NaOH–H_2O fluids (Fig. 4b). The intensity of all bands grows with the increasing temperature and pressure.

The 770–800 cm^{-1} band is assigned to Si–O^- stretch vibrations in isolated SiO_4 tetrahedra (Q^0 species) with one or more of the nonbridging oxygens forming bonds with H^+ (Zotov and Keppler 2002; Mibe et al. 2008). This is the same vibration as that gives rise to a ~ 850 cm^{-1} Raman band in anhydrous silicate melts and glasses (see review of Raman band assignments in such systems by Mysen and Richet 2005). The lower frequency of the Si–O^- stretch vibration in hydrous melts is because of the much smaller radius of H^+ bonded to nonbridging oxygens in the structure compared with alkali metals and alkaline earths. Raman intensity at a higher frequency, as observed in the spectra of SiO_2–H_2O and SiO_2–NaOH–H_2O fluid, is assigned to Si–O^- vibrations in silicate species more polymerized than isolated SiO_4 groups. Most likely, these are species with one bridging oxygen (Q^1 species) (Mysen et al. 2013). Bending vibrations of such a bridge give rise to the intensity centered near 600 cm^{-1}.

It follows, therefore, that for fluids in equilibrium with quartz in the system SiO_2–NaOH–H_2O, the silicate polymerization with Q^0 and Q^1 species is similar

Table 1 Run data

SiO_2–H_2O			SiO_2–NaOH–H_2O			SiO_2–CaO–H_2O		
Temp (°C)[a]	Press (MPa)[b]	Phases	Temp (°C)	Press (MPa)	Phases	Temp (°C)	Press (MPa)	Phases
25	0.1	Qtz + fluid	25	0.1	Qtz + fluid	25	0.1	Qtz + Wo + fluid
550	391	Qtz + fluid	550	583	Qtz + fluid	575	396	Qtz + Wo + fluid
625	542	Qtz + fluid	625	638	Qtz + fluid	625	468	Qtz + Wo + fluid
700	696	Qtz + fluid	700	851	Qtz + fluid	675	498	Qtz + Wo + fluid
775	956	Qtz + fluid	775	1012	Qtz + fluid	725	709	Qtz + Wo + fluid
800	725	Qtz + fluid	800	1134	Qtz + fluid	775	952	Qtz + Wo + fluid
						825	933	Qtz + Wo + fluid

[a]Temperature uncertainty, 2–3 °C
[b]Pressure uncertainty, ± 110 MPa

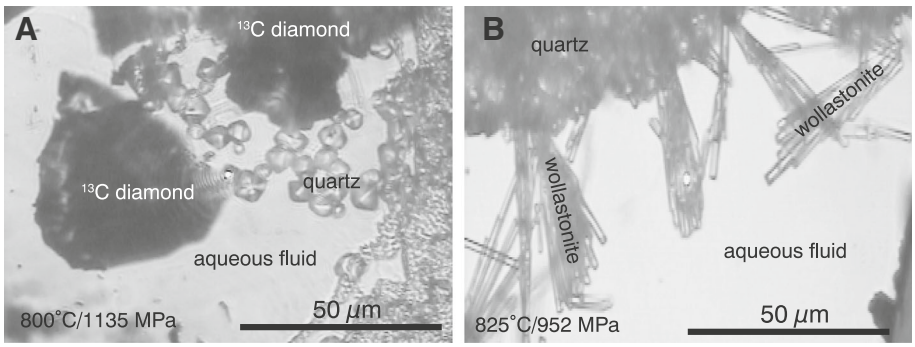

Fig. 1 Examples of microphotographs of samples in the hydrothermal diamond anvil cell at high temperature and pressure. **a** View of the sample from SiO_2–NaOH–H_2O at 800 °C and 1135 MPa. **b** View of the sample from SiO_2–CaO–H_2O at 825 °C and 925 MPa

to that in SiO_2–H_2O fluid spectra at higher pressures (Mysen et al. 2013). It also resembles the aqueous fluids in the equilibrium with alkali aluminosilicate melt under similar temperature and pressure conditions (Mysen 2010).

Discussion

The Raman spectra indicate that the silicate concentration and speciation in the fluid at given temperature and pressure is dependent on the nature of the crystalline materials in the equilibrium with the fluid.

Solubility

Silicate solubility in the aqueous fluids might be estimated by combining silica solubility in the fluid in the system SiO_2–H_2O (Manning 2004) with the intensity of relevant Raman bands in order to generate a calibration curve from the intensity of Raman bands in spectra of

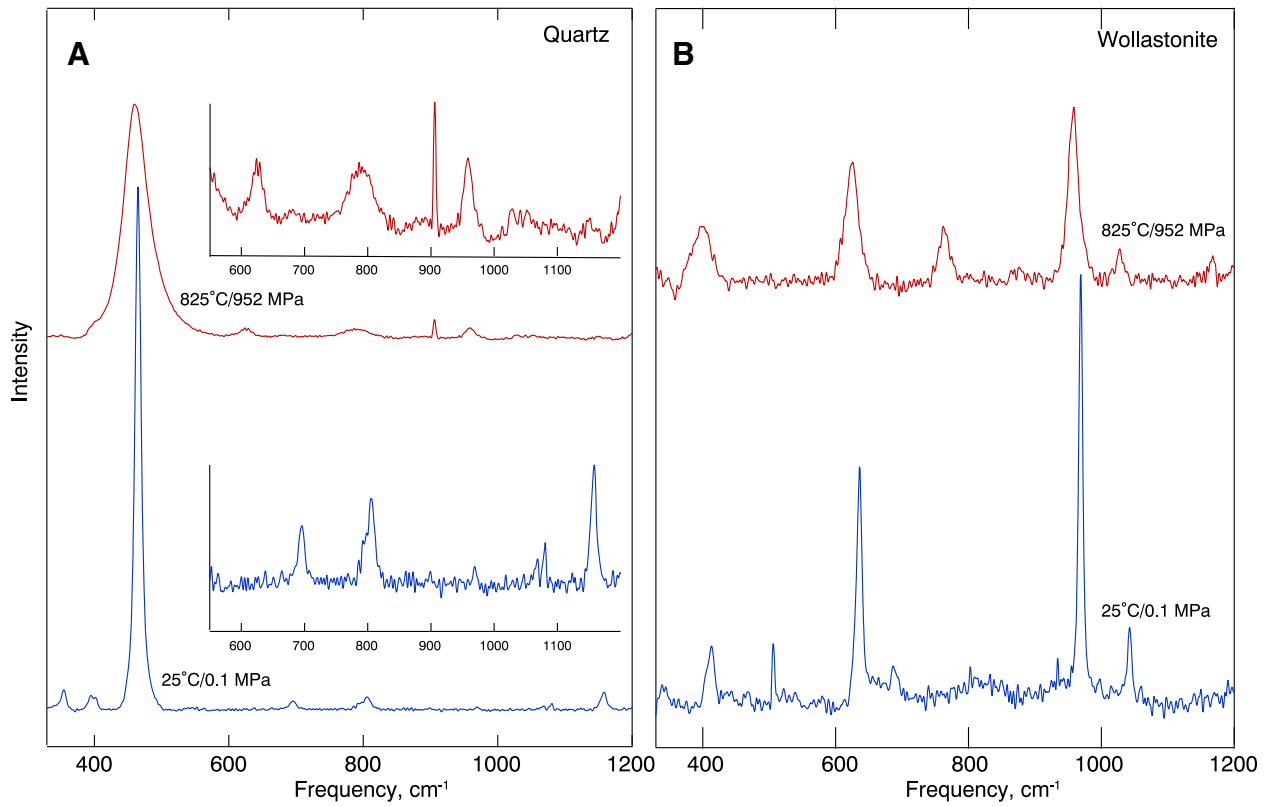

Fig. 2 Raman spectra of crystalline quartz (**a**) and wollastonite (**b**) from the system SiO_2–CaO–H_2O at 825 °C/952 MPa and ambient conditions

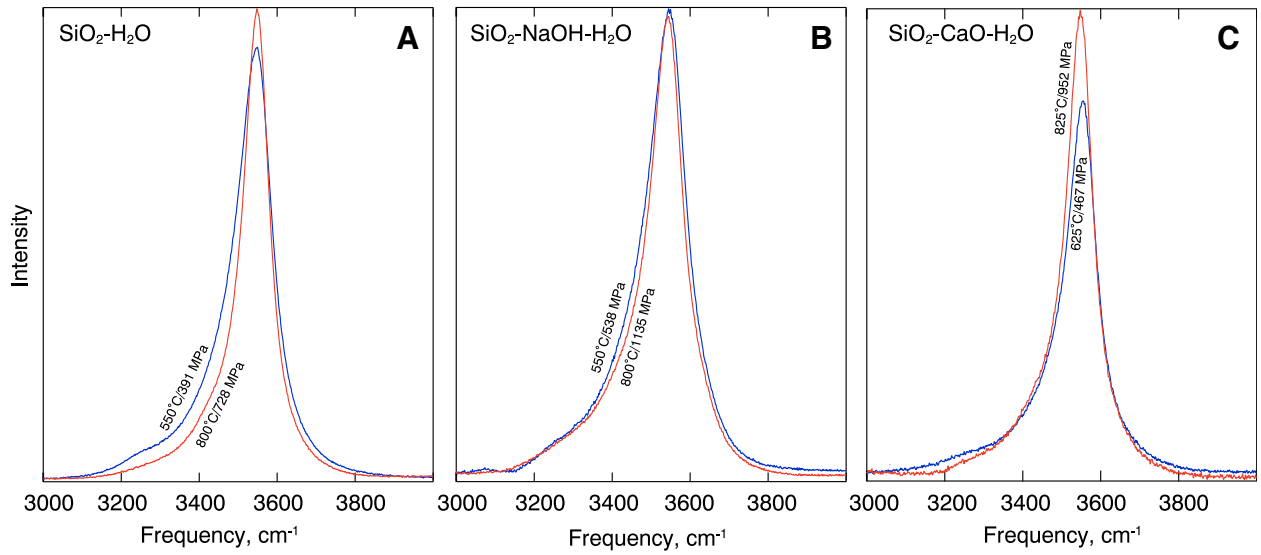

Fig. 3 Examples of high-frequency portion of Raman spectra in the systems SiO_2–H_2O (**a**), SiO_2–NaOH–H_2O (**b**), and SiO_2–CaO–H_2O (**c**) at pressure and temperature conditions as indicated on the individual spectra

fluid. This calibration curve then may be used to compute an approximate solubility of SiO_2 in the fluids from the other two series of experiments (SiO_2–NaOH–H_2O and SiO_2–CaO–H_2O).

The silicate contents of fluid in equilibrium with quartz in the SiO_2–H_2O system were calculated with the algorithm of Manning (1994) in which the temperature and the density of pure H_2O are variables. For the density of the fluid, the calculations by Withers, using the formulism of Pitzer and Sterner (1994), were employed [URL: https://www.esci.umn.edu/people/researchers/withe012/fugacity.htm]. Those SiO_2 solubilities (Table 2) were then used to create a calibration curve based on the 770 + 850 cm^{-1} integrated Raman intensities from the fluid spectra (see Fig. 4). The data points defining the solubility relations were fitted to the function (Fig. 5):

$$\log m_{SiO2}(\mathrm{mol/kg}) = 1.6\text{–}2.0\bullet \mathrm{Int}^{-0.32}(\mathrm{cts/s}), \qquad (1)$$

where "Int" is the integrated intensity of the 770 + 850 cm^{-1} Raman bands in counts per second, and m_{SiO2} is silica molality.

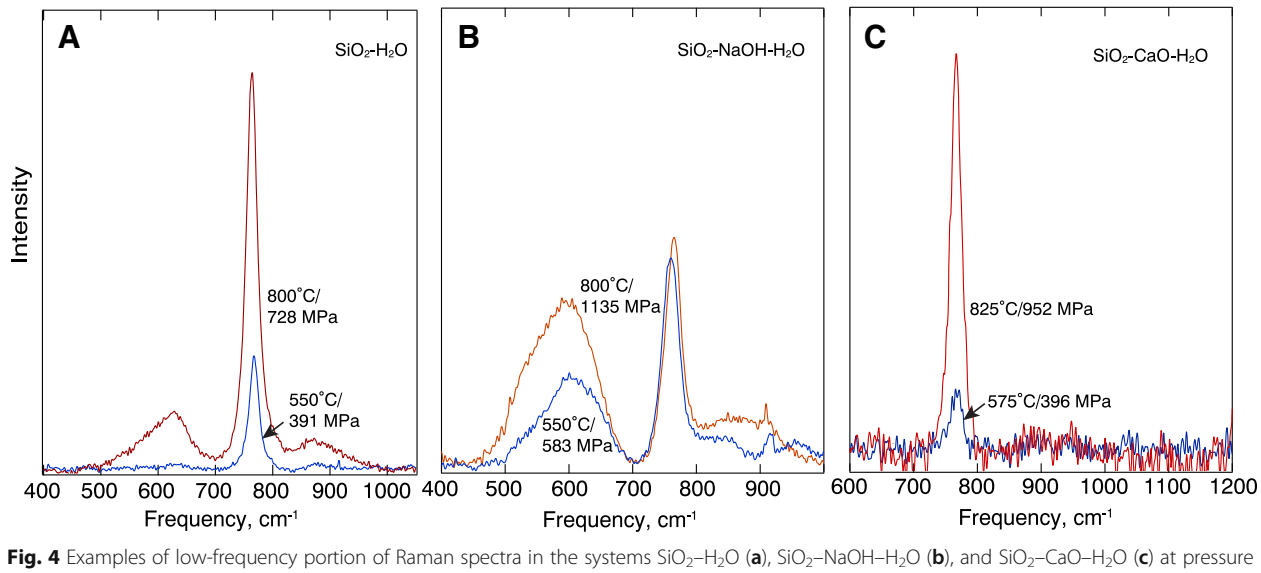

Fig. 4 Examples of low-frequency portion of Raman spectra in the systems SiO_2–H_2O (**a**), SiO_2–NaOH–H_2O (**b**), and SiO_2–CaO–H_2O (**c**) at pressure and temperature conditions as indicated on individual spectra

Table 2 Solubility data

SiO_2–H_2O				
Temp (°C)	Press (MPa)	Density (g/cm^3)	f_{H2O} (MPa)	SiO_2 solubility, m_{SiO2} (kg/mol)[a]
800	728	0.794	852	0.0304
775	956	0.876	1440	0.0273
700	696	0.831	668	0.0082
625	542	0.813	364	0.0022
550	391	0.789	178	0.0004
SiO_2–NaOH–H_2O				
Temp (°C)	Press (MPa)	Density (g/cm^3)	f_{H2O} (MPa)	SiO_2 solubility, m_{SiO2} (kg/mol)[b]
800	1135	0.911	1978	0.0238
775	1012	0.891	1642	0.0448
700	851	0.88	999	0.0288
550	583	0.871	328	0.0092
SiO_2–CaO–H_2O				
Temp (°C)	Press (MPa)	Density (g/cm^3)	f_{H2O} (MPa)	SiO_2 solubility, m_{SiO2} (kg/mol)[b]
575	396	0.775	198	4.86525E−08
625	468	0.779	291	1.43231E−07
675	498	0.764	362	1.38469E−05
725	709	0.824	723	9.61047E−05
775	953	0.875	1430	0.000369701
825	933	0.849	1444	0.000506355

[a]Calculations using the formalism from Manning (1994)
[b]See text for calculations

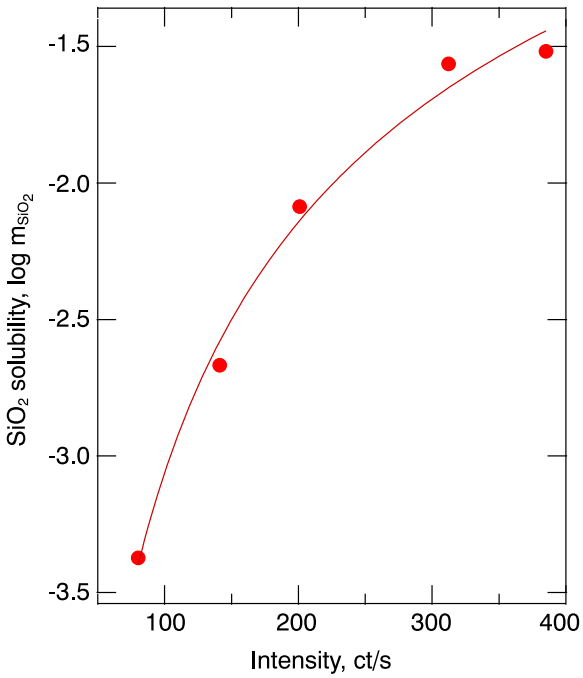

Fig. 5 Calibration curve for SiO_2 solubility as a function of 770 + 850 cm^{-1} integrated band intensity from the system –H_2O with silica solubility calculated with the algorithm of Manning (1994). The fitted curve is log m_{SiO2} (kg/mol) = 1.6–2.0 × Int$^{-0.32}$, where "Int" denotes the integrated Raman intensity and m_{SiO2} is silica molality of aqueous fluid

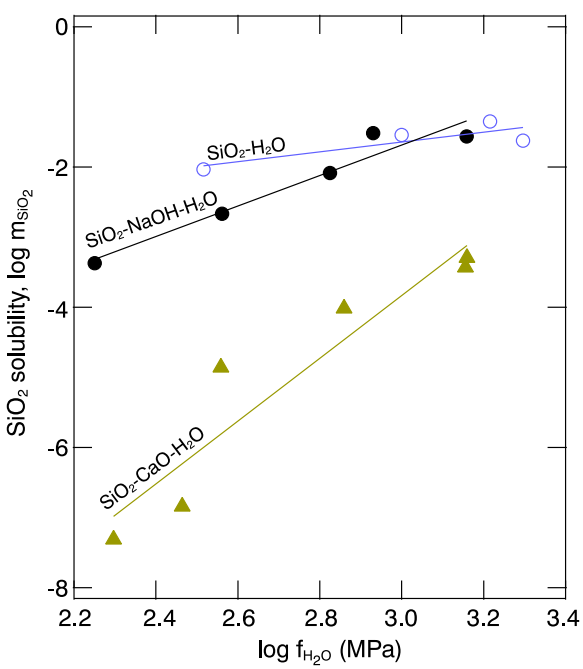

Fig. 6 Silicate solubility in the SiO_2–H_2O, SiO_2–NaOH–H_2O, and SiO_2–CaO–H_2O systems as a function of fugacity of pure H_2O (see text for details of calculations and source of f_{H2O} calculation)

The SiO_2 solubility in the SiO_2–NaOH–H_2O and SiO_2–CaO–H_2O fluids was then derived from the calibration curve in Fig. 6 and the integrated Raman intensities at 770 + 850 cm^{-1} from the SiO_2–NaOH–H_2O and CaO–SiO_2–H_2O fluid spectra. In doing this, it was assumed that the different cations, H^+, Na^+, and Ca^{2+}, in the aqueous solutions had no effect on the Raman intensities and that possible temperature and pressure effects in the pressure range under study on Raman intensity can be ignored.

With the above caveats in mind, the SiO_2 solubility in SiO_2–CaO–H_2O fluids from the calibration curve in Fig. 6 is an order of magnitude, or more, lower than in the SiO_2–NaOH–H_2O and SiO_2–H_2O fluids in the f_{H2O} (H_2O fugacity) range defined by the temperature and pressure conditions of these experiments (Fig. 6; Table 2). The solubility difference does, however, decrease with increasing fugacity of H_2O.

The significant solubility depression resulting from 10 mol% CaO to SiO_2 appears similar to that from MgO in the system MgO–SiO_2–H_2O (Zhang and Frantz 2000). This effect contrasts with adding NaOH where, despite the dilution of SiO_2 concentration, the SiO_2 solubility in aqueous fluids is similar to that in the

simpler SiO_2–H_2O system. The solubility is, however, more sensitive to f_{H2O} in the SiO_2–NaOH–H_2O system so that at high H_2O fugacity, the SiO_2 solubility in the SiO_2–NaOH–H_2O system exceeds that in SiO_2–H_2O fluids (Fig. 6). The temperature/pressure coordinates of the solubility cross-over (750–800 °C at ~ 900 MPa), from linear extrapolation of the curves in Fig. 6, occur at the conditions just below the second critical point in the SiO_2–H_2O system at 1080 °C and 970 MPa (Kennedy et al. 1962). In contrast, linear extrapolation of the SiO_2–CaO–H_2O line leads to a cross-over at an f_{H2O} corresponding to ~ 1300 MPa pressure at 800 °C. These pressure and temperature conditions are inside the supercritical region of the SiO_2–H_2O system, which means that conditions of greater silica solubility in SiO_2–CaO–H_2O fluids than in SiO_2–H_2O and SiO_2–NaOH–H_2O cannot be realized.

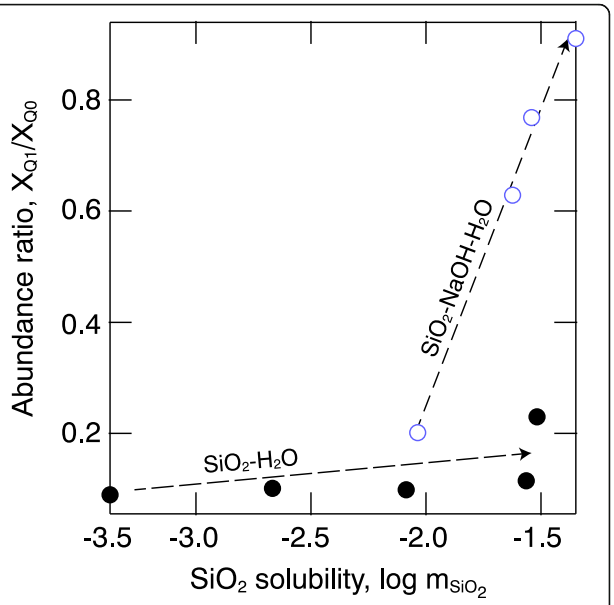

Fig. 7 Silicate species abundance ratio, X_{Q1}/X_{Q0} (X = mol fraction) as a function of SiO_2 solubility (kg/mol)

Silicate speciation in fluid

The approximate concentration of the silicate species in fluid (Q^n species) can be obtained from the integrated intensities of the 770 and 850 cm^{-1} bands of the Raman spectra of fluid. The concentrations thus obtained depend, however, on the assumption that the relative intensities of these two Raman bands are equal to the mol fraction of the species. Given the similar Si–O^- force constants for Si–O^- stretch vibrations in Q^0 and Q^1 in hydrous melts (Cody et al. 2005), the equivalence of relative intensities of the 770 and 850 cm^{-1} bands and the mol fraction of Q^0 and Q^1 species seems a reasonable assumption.

In the SiO_2–H_2O and SiO_2–NaOH–H_2O systems, silica-saturated fluids contain both Q^1 and Q^0 species, whereas in the SiO_2–CaO–H_2O system, only Q^0 species were detected in the temperature and pressure range. For the SiO_2–H_2O and SiO_2–NaOH–H_2O fluids, the Q^0 abundance decreases with increasing temperature and pressure although this decrease is more pronounced in the SiO_2–NaOH–H_2O system. This decrease is coupled with increasing Q^1 abundance. The rate of change of the abundance ratio, X_{Q1}/X_{Q0}, with temperature and pressure is considerably faster in the SiO_2–NaOH–H_2O system and, in fact, can be expressed as linear functions of SiO_2 molality, m_{SiO2} (Fig. 7). Qualitatively, this behavior resembles that for SiO_2–H_2O and SiO_2–MgO–H_2O fluids at pressures above 2 GPa (Mysen et al. 2013). This behavior also is qualitatively similar to that of increased silicate polymerization with increasing total SiO_2 concentration in silicate melts (Buckermann et al. 1992). The difference in silicate species abundance between SiO_2–H_2O and SiO_2–NaOH–H_2O fluids probably occurs because steric hindrance associated with nonbridging oxygen (NBO) bonding to H^+ is greater than Na^+–NBO bonding given the much smaller ionic radius of H^+. Protons will, therefore, favor nonbridging oxygen in Q^0 species, whereas Na^+ will form bonding with nonbridging oxygen in Q^1 species. Hence, the more rapid increase in X_{Q1}/X_{Q0} in the SiO_2–NaOH–H_2O systems than in SiO_2–H_2O.

Thermodynamic considerations

When Q^0 and Q^1 species are present in the fluid, the equilibrium is:

$$2Q^0 \Leftrightarrow Q^1, \tag{2}$$

with the equilibrium constant:

$$K_{(2)} = X_{Q1}/(X_{Q0})^2, \tag{3}$$

where X_{Q1} and X_{Q0} are mol fractions of Q^1 and Q^0, respectively. This equilibrium applies to the SiO_2–H_2O and SiO_2–NaOH–H_2O fluids in the temperature and pressure range discussed here. We note that it differs from that of SiO_2–H_2O at higher pressures (1.8–5.2 GPa) where the silica concentration is sufficiently high to stabilize even more polymerized Q^2 species as well (Mysen et al. 2013).

The silicate speciation in the SiO_2–CaO–H_2O fluids is simpler than in the other two systems as the only species throughout the temperature and pressure is Q^0 only (Fig. 4). Under such circumstances, the

equilibrium constant equals concentration in the fluid, m_{SiO2}:

$$K = m_{SiO2}. \quad (4)$$

From the temperature dependence of the equilibrium constants, the enthalpy change of the reactions follows from:

$$\ln K = -\Delta H/RT + \Delta S/R, \quad (5)$$

where ΔH and ΔS are the enthalpy and entropy changes, T is absolute temperature, and R is the gas constant. It is assumed in using this equation that there is no pressure effect on the equilibria in the pressure range of these experimental results (Table 1). This conclusion is substantiated by the SiO_2–H_2O and SiO_2–MgO–H_2O fluid data of Mysen et al. (2013) who did not detect a pressure dependence in the same pressure range as the present experiments.

A linear fit to ln K versus $1/T$ yields significantly different ΔH values for the equilibria among the Q^n species in the fluid (Fig. 8). For the SiO_2–CaO–H_2O system (Fig. 8a), equilibrium (4) describes the situation. It is more sensitive to temperature ($\Delta H = 322 \pm 4$ kJ/mol) than equilibrium (2), which describes the speciation variations in the SiO_2–H_2O (22 ± 12 kJ/mol) and SiO_2–NaOH–H_2O systems (51 ± 17 kJ/mol; see Fig. 8).

Conclusions

Silicate speciation in silica-saturated aqueous fluids suggested from thermodynamic modeling indicates that species more polymerized than Si $(OH)_4$ type exist in aqueous fluids under pressure/temperature conditions relevant to upper mantle processes (Newton and Manning 2003). This suggestion is consistent with the structural observations reported here and elsewhere (Zotov and Keppler 2002; Mysen et al. 2013). We also note, however, that when NaOH instead of CaO is the third component added to SiO_2–H_2O, the silicate solubility is higher, and both Q^0 and Q^1 species occur in the SiO_2–NaOH–H_2O fluids at lower pressures than in the alkaline earth systems. We note, though, that in these experiments Na^+ was added as an NaOH + H_2O solution. We cannot rule out a contribution to the silicate solubility from the alkaline nature of the fluid such as, for example:

$$2Q^n + 2Na^+ + 2OH^- = 2Q^{n-1} + H_2O, \quad (6)$$

where, therefore, pH would be a contributing factor to the silicate solubility.

Furthermore, as the silicate concentration in aqueous fluids increases and silicate species becomes more polymerized with pressure and temperature, the types and abundance Q^n species more closely resemble those in hydrous silicate melts (Zotov and Keppler 1998; Cody et al. 2005; Mysen 2010). This structural evolution may lead to complete miscibility between silicate and aqueous fluid. It is likely that complete miscibility between fluid and melt occurs at lower pressure in alkali silicate systems than in those of alkaline earth silicate systems because of the greater silicate solubility in alkali silicate fluids. This conclusion accords with experimental observations that show complete miscibility near 1–1.5 GPa in alkali silicate and aluminosilicate systems, whereas pressure exceeds 3 GPa before reaching miscibility in alkaline earth systems (Bureau and Keppler 1999; Stalder et al. 2001; Mibe et al. 2007).

Experimental data indicate that solubility of geochemically important minor and trace elements in aqueous fluids can be significantly affected by other silicate components (Manning 2007; Mysen 2012a, b). This happens because the stability and concentration of minor and trace element complexes (oxy complexes) in fluids depend on the electronic properties of cations available for this purpose in the fluid (Mysen 2012b, 2015b). This means that when considering partitioning of such elements between

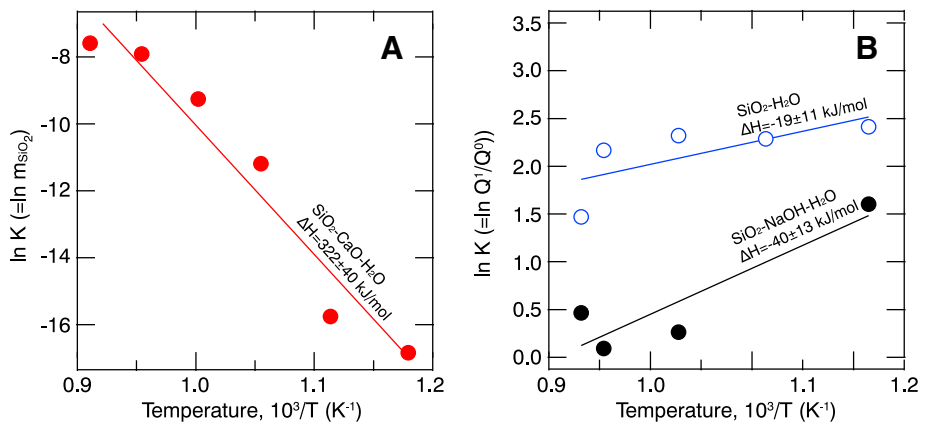

Fig. 8 Equilibrium constants for reactions (4) (**a**) and (2) (**b**) as a function of temperature. The ΔH values are from least squares fit to Eq. (3)

minerals and aqueous fluids in the upper mantle and deep crust, pressure-dependent partition coefficients likely reflect changing silicate-cation interaction in the fluid as a function of silicate solubility and speciation.

Qualitatively, this behavior also means that for fluids in equilibrium with mafic and ultramafic mineral assemblages where alkaline earths are dominating cations, the silicate solubility in fluid is less and silicate polymerization is less extensive than in fluids in the equilibrium in felsic systems such as typical gneiss compositions, for example, where alkali metals are more important. Moreover, because the fluid composition in equilibrium with such different crystalline rocks differs, minor and trace element complexing in those different fluids also differs, which leads to different fluid-melt-crystal partition coefficients as a function of rock type (mineral assemblage) with which aqueous fluids equilibrated.

Abbreviations

ΔH: Enthalpy change; ΔS: Entropy change; CCD: Charge-coupled detector; f_{H2O}: H_2O fugacity; HDAC: Hydrothermal diamond anvil cell; HFSE: High field strength element; m_{SiO2}: SiO_2 molality; R: Gas constant; X_{Q0}: Mol fraction of Q^0 species; X_{Q1}: Mol fraction of Q^1 species

Acknowledgements

Instrument, electronics, and library support was provided by Geophysical Laboratory technical staff. Their support is gratefully acknowledged.

Funding

This research was supported by grant EAR1212854 from the National Science Foundation.

Availability of data and materials

The data used are reported in the manuscript tables. All original data are available from the author on request.

Authors' contributions

All research reported in this report was carried out by the author. The author read and approved the final manuscript.

Competing interests

The author declares that he has no competing interests.

Publisher's Note

Received: 16 May 2018 Accepted: 19 July 2018
Published online: 14 August 2018

References

Bassett WA, Shen AH, Bucknum M, Chou IM (1993) A new diamond cell for hydrothermal studies to 2.5 GPa and from -190°C to 1200°C. Rev Sci Instrum 64:2340–2345. https://doi.org/10.1063/1.1143931

Brawer SA, White WB (1975) Raman spectroscopic investigation of the structure of silicate glasses. I. The binary silicate glasses. J Chem Phys 63:2421–2432. https://doi.org/10.1063/1.431671

Buckermann WA, Muller-Warmuth W, Frischat GH (1992) A further 29Si MAS NMR study on binary alkali silicate glasses. Glasstech Ber 65:18–21

Burchard M, Maresch WV, Fockenberg T, Doltsinis NL, Adeagbo WA (2011) Modelling high-pressure aqueous fluids in the system CaO-SiO_2-H_2O: a comprehensive semi-empirical thermodynamic formalism. Eur J Mineral 23: 409–424. https://doi.org/10.1127/0935-1221/2011/0023-2106

Bureau H, Keppler H (1999) Complete miscibility between silicate melts and hydrous fluids in the upper mantle; experimental evidence and geochemical implications. Earth Planet Sci Lett 165:187–196. https://doi.org/10.1016/S0012-821X(98)00266-0

Cody GD, Mysen BO, Lee SK (2005) Structure vs. composition: a solid-state H-1 and Si-29 NMR study of quenched glasses along the Na_2O-SiO_2-H_2O join. Geochim Cosmochim Acta 69:2373–2384. https://doi.org/10.1016/j.gca.2004.11.012

Fockenberg T, Burchard M, Maresch VW (2006) Experimental determination of the solubility of natural wollastonite in pure water up to pressures of 5 GPa and at temperatures of 400-800 degrees C. Geochim Cosmochim Acta 70: 1796–1806. https://doi.org/10.1016/j.gca.2005.12.017

Kawamoto T, Kanzaki M, Mibe K, Matsukage KN, Ono S (2012) Separation of supercritical slab-fluids to form aqueous fluid and melt components in subduction zone magmatism. Proc Natl Acad Sci USA 109:18695–18700. https://doi.org/10.1073/pnas.1207687109

Kennedy GC, Wasserburg GJ, Heard HC, Newton RC (1962) The upper three-phase region in the system SiO_2-H_2O. Am J Sci 260:501–521. https://doi.org/10.2475/ajs.260.7.501

Kessel R, Schmidt MW, Ulmer P, Pettke T (2005) Trace element signature of subduction-zone fluids, melts and supercritical liquids at 120-180 km depth. Nature 437:724–727. https://doi.org/10.1038/nature03971

Kessel R, Ulmer P, Pettke T, Schmidt MW, Thompson AB (2004) A novel approach to determine high-pressure high-temperature fluid and melt compositions using diamond-trap experiments. Am Mineral 89:1078–1086

Manning CE (1994) The solubility of quartz in H_2O in the lower crust and upper mantle. Geochim Cosmochim Acta 58:4831–4840. https://doi.org/10.1016/0016-7037(94)90214-3

Manning CE (2004) The chemistry of subduction-zone fluids. Earth Planet Sci Lett 223:1–16. https://doi.org/10.1016/j.epsl.2004.04.030

Manning CE (2007) Solubility of corundum+kyanite in H_2O at 700°C and 10 kbar: evidence for Al-Si complexing at high pressure and temperature. Geofluids 7: 258–268. https://doi.org/10.1111/j.1468-8123.2007.00179.x

Manning CE, Boettcher S (1994) Rapid quench hydrothermal experiments at mantle pressures and temperatures. Am Mineral 79:1153–1158

McMillan PF, Wolf GH, Poe BT (1992) Vibrational spectroscopy of silicate liquids and glasses. Chem Geol 96:351–366. https://doi.org/10.1016/0009-2541(92)90064-C

Mibe K, Chou IM, Bassett WA (2008) In situ Raman spectroscopic investigation of the structure of subduction-zone fluids. J Geophys Res 113. https://doi.org/10.1029/2007jb005179

Mibe K, Kanzaki M, Kawamoto T, Matsukage KN, Fei Y, Ono S (2007) Second critical endpoint in the peridotite-H_2O system. J Geophys Res 112. https://doi.org/10.1029/2005JB004125

Mibe, K., Kawamoto, T., Matsukage, K.N., Fei, Y., and Ono, S. (2011) Slab melting versus slab dehydration in subduction-zone magmatism. Proc. Nat'l. Acad. Sci. https://doi.org/10.1073/pnas.1010968108

Mysen BO (2010) Structure of H_2O-saturated peralkaline aluminosilicate melt and coexisting aluminosilicate-saturated aqueous fluid determined in-situ to 800 C and 800 MPa. Geochim Cosmochim Acta 74:4123–4139. https://doi.org/10.1016/j.gca.2010.04.024

Mysen BO (2012a) Silicate-COH melt and fluid structure, their physicochemical properties, and partitioning of nominally refractory oxides between melts and fluids. Lithos 148:228–246. https://doi.org/10.1016/j.lithos.2012.06.005

Mysen BO (2012b) High-pressure/-temperature titanium solution mechanisms in silicate-saturated aqueous fluids and hydrous silicate melts. Am Mineral 97: 1241–1251. https://doi.org/10.2138/am.2012.4084

Mysen BO (2015a) Carbon speciation in silicate-C-O-H as a function of redox conditions: an experimental study, in-situ to 1.7 GPa and 900°C. Am Mineral 100:872–882. https://doi.org/10.2138/am-2015-4976

Mysen BO (2015b) An in-situ experimental study of Zr^{4+} transport capacity of water-rich fluids in the temperature and pressure range of the deep crust and upper mantle. Prog Earth Planet Sci 2(1):38. https://doi.org/10.1186/s40645-015-0070-5

Mysen BO, Mibe K, Chou IM, Bassett WA (2013) Structure and equilibria among silicate species in aqueous fluids in the upper mantle: experimental SiO_2-H_2O and MgO-SiO_2-H_2O data recorded in situ to 900 degrees C and 5.4GPa. J Geophys Res 118:6076–6085. https://doi.org/10.1002/2013jb010537

Mysen BO, Richet P (2005) Silicate glasses and melts—properties and structure. Elsevier, New York, p 548

Mysen BO, Yamashita S (2010) Speciation of reduced C-O-H volatiles in coexisting fluids and silicate melts determined in-situ to ~1.4 GPa and 800°C. Geochim Cosmochim Acta 74:4577–4588

Newton RC, Manning CE (2002) Solubility of enstatite+forsterite in H_2O in deep crust/upper mantle conditions: 4 to 15 kbar and 700 to 900°C. Geochim Cosmochim Acta 66:4165–4176. https://doi.org/10.1016/S0016-7037(02)00998-5

Newton RC, Manning CE (2003) Activity coefficient and polymerization of aqueous silica at 800°C, 12 kbar, from solubility measurements and SiO_2-buffering mineral assemblages. Contrib Mineral Petrol 146:135–146. https://doi.org/10.1007/s00410-003-0483-9

Newton RC, Manning CE (2009) Hydration state and activity of aqueous silica in H_2O-CO_2 fluids at high pressure and temperature. Am Mineral 94:1287–1290. https://doi.org/10.2138/am.2009.3287

Osborn EF, Muan A (1960) Plate 2. The system CaO-MgO-SiO_2: phase equilibrium diagrams of oxide systems. American Ceramic Society

Pitzer KS, Sterner SM (1994) Equations of state valid continuously from zero to extreme pressures for H_2O and CO_2. J Chem Phys 101:3111–3116. https://doi.org/10.1063/1.467624

Ratcliffe CI, Irish DE (1982) Vibrational studies of solutions at elevated temperatures and pressures. 5. Raman studies of liquid water up to 300 °C. J Phys Chem 86:4897–4905. https://doi.org/10.1021/j100222a013

Stalder R, Ulmer P, Thompson AB, Gunther D (2001) High pressure fluids in the system MgO-SiO_2-H_2O under upper mantle conditions. Contrib Mineral Petrol 140:607–618. https://doi.org/10.1007/s004100000212

Walrafen GE, Fisher MR, Hokmabadi MS, Yang WH (1986) Temperature dependence of the low- and high-frequency Raman scattering from liquid water. J Chem Phys 85:6970–6982. https://doi.org/10.1063/1.451384

Wilke M, Schmidt C, Dubrail J, Appel K, Borchert M, Kvashnina K, Manning CE (2012) Zircon solubility and zircon complexation in H_2O+Na_2O+SiO_2±Al_2O_3 fluids at high pressure and temperature. Earth Planet Sci Lett 349-350:15–25. https://doi.org/10.1016/j.epsl.2012.06.054

Zhang Y-G, Frantz JD (2000) Enstatite-forsterite-water equilibria at elevated temperatures and pressures. Am Mineral 85:918–925. https://doi.org/10.2138/am-2000-0705

Zotov N, Keppler H (1998) The influence of water on the structure of hydrous sodium tetrasilicate glasses. Am Mineral 83:823–834

Zotov N, Keppler H (2002) Silica speciation in aqueous fluids at high pressures and high temperatures. Chem Geol 184:71–82. https://doi.org/10.1016/S0009-2541(01)00353-9